nature chemistry

ARTICLES

https://doi.org/10.1038/s41557-022-00915-2

Check for updates

In situ multiscale probing of the synthesis of a Ni-rich layered oxide cathode reveals reaction heterogeneity driven by competing kinetic pathways

Hyeokjun Park[1,2,8,9], Hayoung Park[2,3,9], Kyung Song[4], Seok Hyun Song[5], Sungsu Kang[2,3], Kun-Hee Ko[1], Donggun Eum[1], Yonggoon Jeon[2,3], Jihoon Kim[2,3], Won Mo Seong[1], Hyungsub Kim[5], Jungwon Park[2,3,6,7] ✉ and Kisuk Kang[1,2,3,6] ✉

Nickel-rich layered oxides are envisaged as key near-future cathode materials for high-energy lithium-ion batteries. However, their practical application has been hindered by their inferior cycle stability, which originates from chemo-mechanical failures. Here we probe the solid-state synthesis of $LiNi_{0.6}Co_{0.2}Mn_{0.2}O_2$ in real time to better understand the structural and/or morphological changes during phase evolution. Multi-length-scale observations—using aberration-corrected transmission electron microscopy, in situ heating transmission electron microscopy and in situ X-ray diffraction—reveal that the overall synthesis is governed by the kinetic competition between the intrinsic thermal decomposition of the precursor at the core and the topotactic lithiation near the interface, which results in spatially heterogeneous intermediates. The thermal decomposition leads to the formation of intergranular voids and intragranular nanopores that are detrimental to cycling stability. Furthermore, we demonstrate that promoting topotactic lithiation during synthesis can mitigate the generation of defective structures and effectively suppress the chemo-mechanical failures.

Nickel-rich lithium layered oxides have received tremendous attention as the most promising cathode materials for the practical development of high-energy lithium-ion batteries. Unlike with conventional cobalt-based layered oxides, the practical capacity of which remains far below the theoretical value, the high nickel content in lithium nickel–cobalt–manganese layered oxides ($LiNi_xCo_yMn_zO_2$ (NCM), $x+y+z=1$, $x\geq 0.6$) enables the utilization of the near-theoretical specific capacity of the layered transition-metal oxides in conventional lithium-ion battery systems while reducing the use of expensive and toxic cobalt[1–5]. Nevertheless, nickel-rich NCM electrodes commonly suffer from rapid capacity decay during cycling, coupled with structural and morphological degradation. Various degradation mechanisms of NCM materials have been explored including side reactions with electrolytes[6], irreversible phase transformation[7,8], transition-metal dissolution[9,10] and oxygen release[11,12], all of which are complicatedly intertwined with one another. Extensive studies have also unravelled that the failure mechanism involves the mechanical deterioration of electrode particles by microcracking in secondary particles due to the build-up of large anisotropic strains during phase transition and the chemical parasitic reactions with electrolytes via the crevice created[13–17]. Such chemo-mechanical failures were also found to be easily triggered or aggravated by various structural defects, including internal void spaces[8,18–20], surface reconstruction layers[21–25] and intragranular nanopores[26–31]. These defective structures, detrimental to the electrochemical properties, have been commonly observed in the primary and secondary particles of conventionally synthesized nickel-rich NCM materials. Thus, some efforts have recently been made to explore single-crystalline particles without the extrinsic defects, such as grain boundaries, formed during the conventional coprecipitation-based synthesis, with partial success in improving the cycle stability[32,33]. However, regardless of whether the particles are single-crystalline or poly-crystalline, fundamental questions concerning the general defect formations still need to be addressed for this material in terms of how the defects are formed during the intrinsic synthetic process from the precursor to the final product stage and how these defects affect the electrochemical degradation. Direct investigation of the defect formation processes in nickel-rich NCM would provide insight for the design of layered electrode materials with enhanced structural integrity that can alleviate defect-induced failure during cycling and improve the long-term stability.

So far, our mechanistic understanding of NCM materials has primarily relied on post-mortem analyses, which have provided important evidence of the structure–property correlation in electrode materials[2,5,23,34,35]. Although these approaches are easily accessible

[1]Department of Materials Science and Engineering & Research Institute of Advanced Materials (RIAM), Seoul National University, Seoul, Republic of Korea. [2]Center for Nanoparticle Research, Institute for Basic Science (IBS), Seoul National University, Seoul, Republic of Korea. [3]School of Chemical and Biological Engineering, and Institute of Chemical Process, Seoul National University, Seoul, Republic of Korea. [4]Department of Materials Modeling and Characterization, Korea Institute of Materials Science, Changwon, Republic of Korea. [5]Neutron Science Center, Korea Atomic Energy Research Institute (KAERI), Daejeon, Republic of Korea. [6]Institute of Engineering Research, College of Engineering, Seoul National University, Seoul, Republic of Korea. [7]Advanced Institutes of Convergence Technology, Seoul National University, Suwon-si, Republic of Korea. [8]Present address: Korea Research Institute of Standards and Science, Daejeon, Republic of Korea. [9]These authors contributed equally: Hyeokjun Park, Hayoung Park. ✉e-mail: jungwonpark@snu.ac.kr; matlgen1@snu.ac.kr

and effective in revealing certain key properties, they are prone to overlooking important information concerning non-equilibrium intermediate states and/or the reaction kinetics of the target chemical process. Several recent approaches have thus used in situ diffraction techniques to study the reaction pathway in real time by tracking the structural evolution of certain layered oxide materials during solid-state synthesis[32,35–41], which reveals the presence of metastable intermediate phases during the dynamic synthetic process[39,40]. Nevertheless, such an in situ investigation based on diffraction provides the average crystallographic information for the bulk structure and fails to explain how the spatially inhomogeneous reaction begins at the interface of reacting precursors and propagates during the synthesis, which is crucial for elucidating the synthetic mechanism of NCM formation and the development of defect structures.

In this Article, we scrutinize the synthesis mechanism of a representative NCM material, $LiNi_{0.6}Co_{0.2}Mn_{0.2}O_2$ (NCM622), from the conventional coprecipitated precursors using a combination of high-end analysis methods, including aberration-corrected transmission electron microscopy (TEM), in situ heating TEM with gas control and in situ X-ray diffraction. Multi-scale in situ examinations are employed in probing the synthesis of the NCM622 with broad spatial resolution from the subnanometre to micrometre scale to better understand the internal crystal structure evolution and the associated morphology changes of micro-sized NCM particles. Comparative investigations of synthetic conditions reveal that kinetic competitions between the self-decomposition of precursors and the topotactic lithiation of the transition-metal hydroxide (TM precursor), whose dominance is dependent on the thermal reactivity of different lithium precursors. The spatially resolved TEM study further demonstrates that the topotactic formation of the layered oxide readily occurs at the interface between the TM precursor and the lithium precursor, whereas the thermal decomposition of the TM precursor dominates in the particle core. These two competing reactions leave radially heterogeneous non-equilibrium intermediates in the secondary particle. More importantly, the self-decomposition of the TM precursor is accompanied by the substantial formation of structural defects including (1) intergranular voids in secondary particles and (2) intragranular nanopores in primary particles. This mechanistic understanding guides us to develop a new quasi-equilibrium synthetic route for NCM622 that effectively mitigates the formation of these defects, thereby improving the long-term cycle stability of the electrode. This work highlights the importance of multiscale probing of the real-time reaction process and the control of intrinsic structural defects in elucidating the chemo-mechanical properties of NCM electrodes.

Results and discussion

Near-equilibrium synthetic pathway. We first examined the phase evolution of the precursor mixture of the transition-metal hydroxide ($TM(OH)_2$) and lithium hydroxide (LiOH) upon heating using ex situ X-ray diffraction (Extended Data Fig. 1). The mixtures of the precursor phases were observable below 300 °C with simultaneous decomposition of the LiOH and notable evolution of the Bragg reflections related to the layered structure above 400 °C, which is consistent with previous results[37,40,41]. However, the relatively fast ramping rate of the conventional heating protocol makes the assignment of the near-equilibrium or intermediate phases at each temperature ambiguous. We thus modified the heat profile in our in situ X-ray diffraction study to clarify the phase evolutions in the near-equilibrium synthetic pathway (Supplementary Fig. 1). Interestingly, we found that the main Bragg reflection of the $TM(OH)_2$ near 19.5° gradually shifts toward the 003 Bragg reflection of the $R\bar{3}m$ layered oxide at 18.5° starting at a temperature of as low as ~200 °C, as shown in Fig. 1a, implying the continuous phase transition from layered hydroxide to layered lithium oxide, which resembles the topotactic lithiation of layered electrode materials[42]. The evolving phase fraction was quantitatively assessed by results of Rietveld refinements based on the diffraction patterns in Fig. 1b. The results confirm that the conversion from the $TM(OH)_2$ to the pseudo layered oxide, possibly with partial disordering or stacking faults, mainly occurs at 200–250 °C along with the disappearance of LiOH. Beyond that temperature, the diffraction patterns of the $R\bar{3}m$ layered oxide tend to become sharp and intensified (Fig. 1a), inferring the progress of structural ordering in the layered NCM. The progress of the structural ordering in the layered NCM is also supported by the quantification of the amount of the Li/Ni cation disordering from the refinement, which is maximum at 300 °C and continuously decreases with heating (bottom panel in Fig. 1b)[35,37,43]. These observations indicate that the direct transition occurs from the layered $TM(OH)_2$ to the NCM pseudo layered oxide at an unexpectedly low temperature, via the topotactic lithiation.

The TEM study further confirms the direct transition to the layered oxide at a substantially low temperature. Figure 1c–e presents cross-sectional scanning electron microscopy (SEM) images of the precursors heated at 200, 250 and 300 °C along the quasi-equilibrium synthetic pathway, respectively. The figure clearly illustrates that even the sample heated to only 200 °C adopted the layered NCM oxide structure, as verified by the nanobeam diffraction (NBD) patterns. While the inner particle contained unreacted $TM(OH)_2$ precursor (Fig. 1f), the outer shell of the precursor had already transformed to the typical layered oxide structure (Fig. 1i), signifying that the lithiation process progresses from the outer to the inner part of the $TM(OH)_2$ particles. At the slightly higher temperatures of 250 and 300 °C, all the NBD patterns correspond to the layered oxide phase over the entire region of the particle (Fig. 1g,h,j,k), which is consistent with the X-ray diffraction results.

To further understand the thermal behaviours of the precursors upon heating, we performed differential thermal analysis (DTA) and thermal gravimetric analysis (TGA), as shown in Fig. 1l. The pristine $TM(OH)_2$ (top panel) undergoes exothermic events with a notable weight loss from approximately 220 °C to 350 °C, which is attributable to the decomposition reaction of the $TM(OH)_2$ into the oxide[44–46] and is consistent with our ex situ X-ray diffraction results in Supplementary Fig. 2. On the other hand, the DTA–TGA curves of the mixture with the LiOH feature a preceding thermal event near 200 °C, as indicated by the arrow in Fig. 1l (bottom panel), before the decomposition of the $TM(OH)_2$. This additional exothermic reaction is attributed to the early synthetic lithiation into the $TM(OH)_2$ and supports the idea that the topotactic lithiation can be driven by LiOH at the relatively low temperature of ~200 °C. This process contrasts with the case of the precursor mixture with lithium carbonate (Li_2CO_3), another common lithium source for the synthesis of layered oxide. It was found that the thermal decomposition of the pristine $TM(OH)_2$ precedes and is followed by the lithiation reaction at approximately 400 °C (Extended Data Fig. 2 and Supplementary Fig. 3). The typical decomposition of the $TM(OH)_2$ is accompanied by the loss of the hydroxide bond, inevitably involving substantial atomic rearrangements into the rock-salt structure; however, this transition is compensated for in the presence of the LiOH by the subsequent site occupancy of lithium ions without considerable structural rebuilding. The onset temperatures of the lithiation (~200 °C) and thermal decomposition (~220 °C) of the $TM(OH)_2$ are remarkably similar, hinting at the critical role of the LiOH in triggering the early transition to the layered transition-metal oxide by lithiation. As nickel-rich layered oxides are highly vulnerable to structural disordering induced at high temperature, such as cation mixing, it is presumed that the early topotactic lithiation induced by the use of LiOH is highly beneficial for the structural development of the layered oxide. This result rehighlights the preferred use of LiOH over Li_2CO_3 for the synthesis of nickel-rich layered oxides (Supplementary Note 1)[5,47–49].

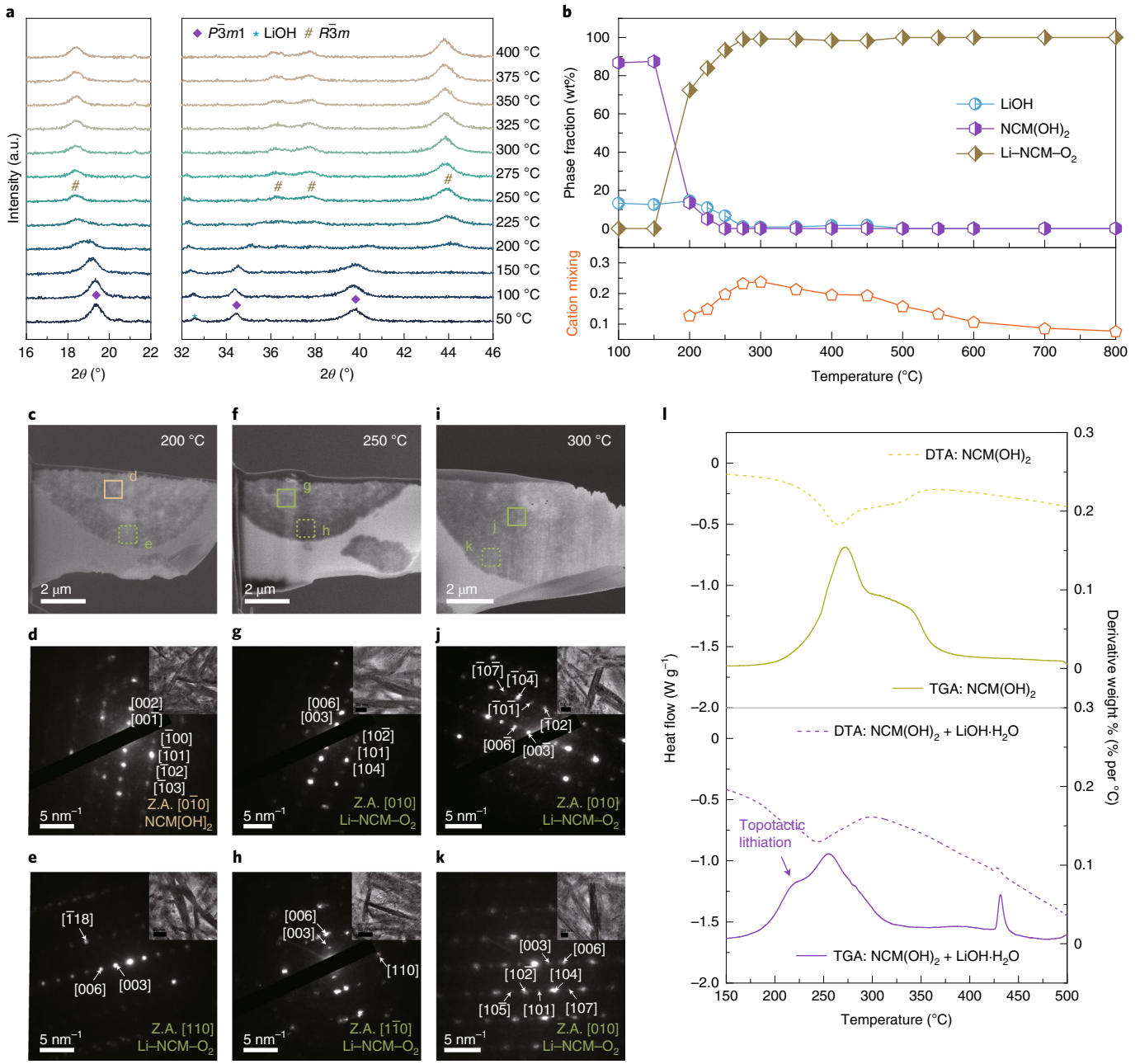

Fig. 1 | Topotactic lithiation into layered $TM(OH)_2$ precursor at low temperature. a, In situ X-ray diffraction pattern at given equilibrated temperature for calcinations of precursors for transition-metal layered oxide. θ is the angle between the incident beam and the crystallographic reflecting plane. 2θ roots from the powder diffraction based on Bragg–Brentano geometry ($\theta - 2\theta$). **b**, Phase and structural evolution during the synthesis. **c**–**k**, Cross-sectional SEM images and NBD patterns with TEM images (inset) of heated samples at 200 °C (**c**–**e**), 250 °C (**f**–**h**) and 300 °C (**i**–**k**). Z.A., zone axis. **l**, TGA (solid line) and DTA (dotted line) curves of $TM(OH)_2$ (top) and its composite with LiOH (bottom). Differential curve for TGA is presented. The purple arrow and exothermal peak at 430 °C in the bottom panel correspond to topotactic lithiation of $TM(OH)_2$ and the decomposition of LiOH, respectively.

Kinetic intermediates with phase and morphology heterogeneity. Based on the information of the near-equilibrium reaction pathways, we comparatively studied the effect of the kinetic limitation in the conventional synthetic routes of nickel-rich NCM and its influence on the external defect formation. The comparative reaction kinetics were believed to be important in this case, especially because the onset temperatures of the synthetic lithiation and the thermal decomposition of the $TM(OH)_2$ were close to each other, as shown in the previous section. The real-time monitoring of the reaction was thus performed by employing in situ environmental heating TEM mimicking the realistic synthetic conditions of nickel-rich layered oxides. Figure 2a illustrates the scheme of a nanoreactor for the synthesis with controlled heating and oxygen environments. Figure 2b depicts the pristine state of the precursors, in which the needle-like agglomerates of $TM(OH)_2$ are observable by the dark contrast. Upon heating the nanoreactor, a noticeable change was observed in the particle up to 300 °C, as presented in the time-series TEM images in Fig. 2c. Interestingly, a boundary begins to form inside the secondary particle from approximately 240 °C, resulting in a core–shell-like structure at 300 °C (Fig. 2d; real-time video in Supplementary Video 1). The formation of the core–shell is further verified by the intensity analyses of TEM images

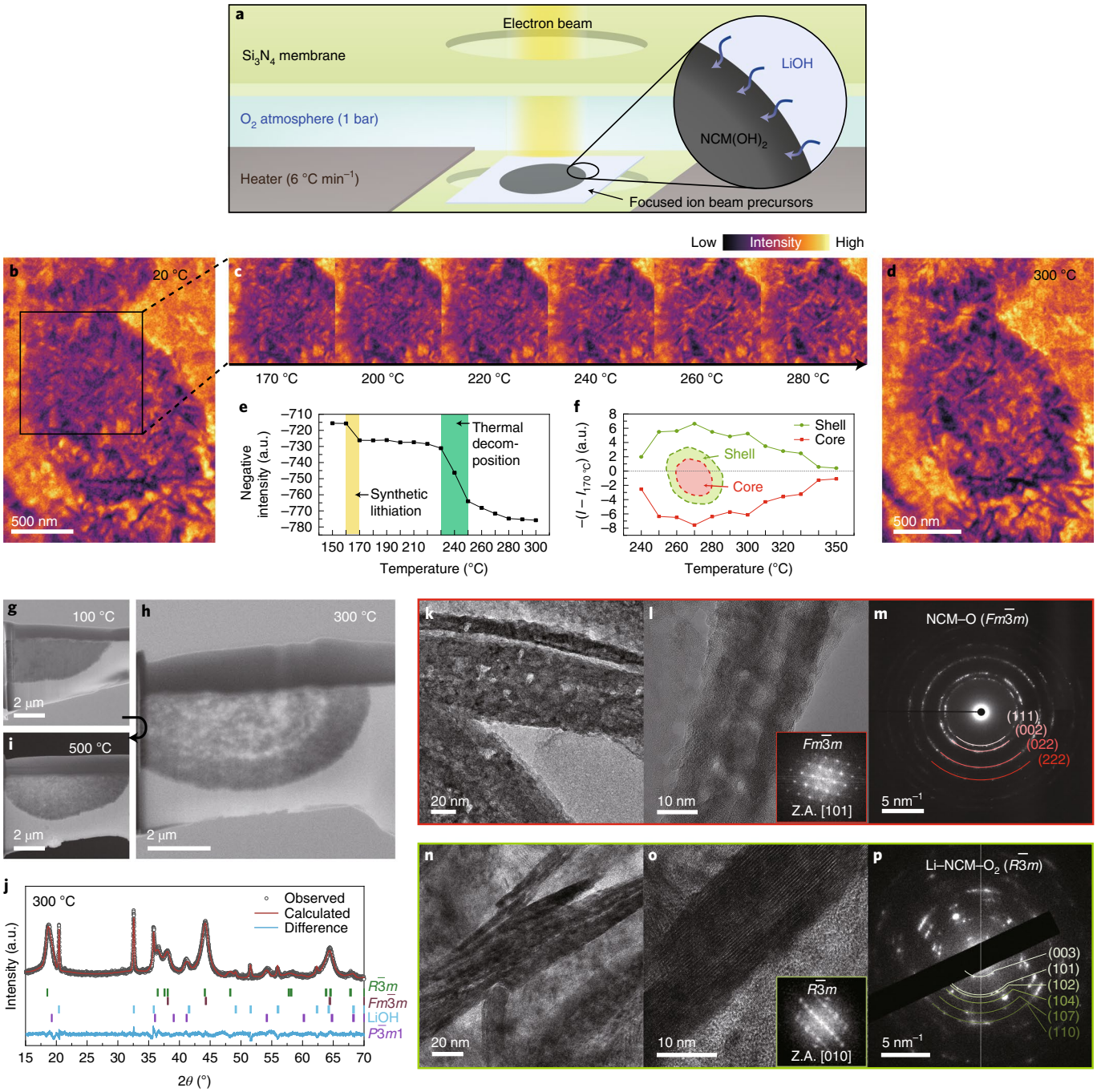

Fig. 2 | Heterogeneous phase evolution at low-temperature intermediate by kinetic competition. a, Graphical illustration of environmental heating of TEM chips. The detailed specifications of the nanoreactor and sample preparation are provided in Methods. **b**, TEM image of pristine precursor specimen. **c**, In situ TEM images during heating. **d**, TEM image of samples heated to 300 °C with core–shell boundary. The TEM images are colour-coded after image processing, the details of which are provided in Supplementary Note 2. **e**, Total negative intensity profile during heating. The negative intensity is proportional to the mass of the specimen. **f**, Averaged negative intensity change of the core and shell regions during heating. The inset presents a schematic of the analysis model. The negative intensity (I) changes are presented relatively for the core and shell regions with respect to the intensities at 170 °C ($I_{170\,°C}$). **g**–**i**, Cross-sectional SEM images of samples annealed ex situ at 100 °C (**g**), 300 °C (**h**) and 500 °C (**i**). **j**, Refined X-ray diffraction patterns of 300 °C sample resolving heterogeneity in phase. The sample consists of the layered $R\bar{3}m$ (Li-TM-O_2, green, 69.7%), $Fm\bar{3}m$ rock salt (TM-O, red, 19.5%) and $P\bar{3}m1$ unreacted precursor (TM$(OH)_2$, purple, 10.9%). **k**–**m**, TEM images (**k**,**l**) and selected-area electron diffraction pattern (**m**) of core region for 300 °C sample. **n**–**p**, TEM images (**n**,**o**) and selected-area electron diffraction pattern (**p**) of shell region for 300 °C sample. The inset images in **l** and **o** are the fast Fourier transform pattern for the TEM image. The spots for **k**–**p** within the secondary particle are presented in the Supplementary Information.

(Supplementary Note 2). Overall, the negative intensity of the particle in Fig. 2e decreases upon heating at the temperature range of interest, which corresponds to the weight loss as observed in the DTA–TGA analysis. However, the relative change in the intensity indicates the distinct behaviours in the core and shell regions of the particle (Fig. 2f). The shell region becomes denser due to the gain in

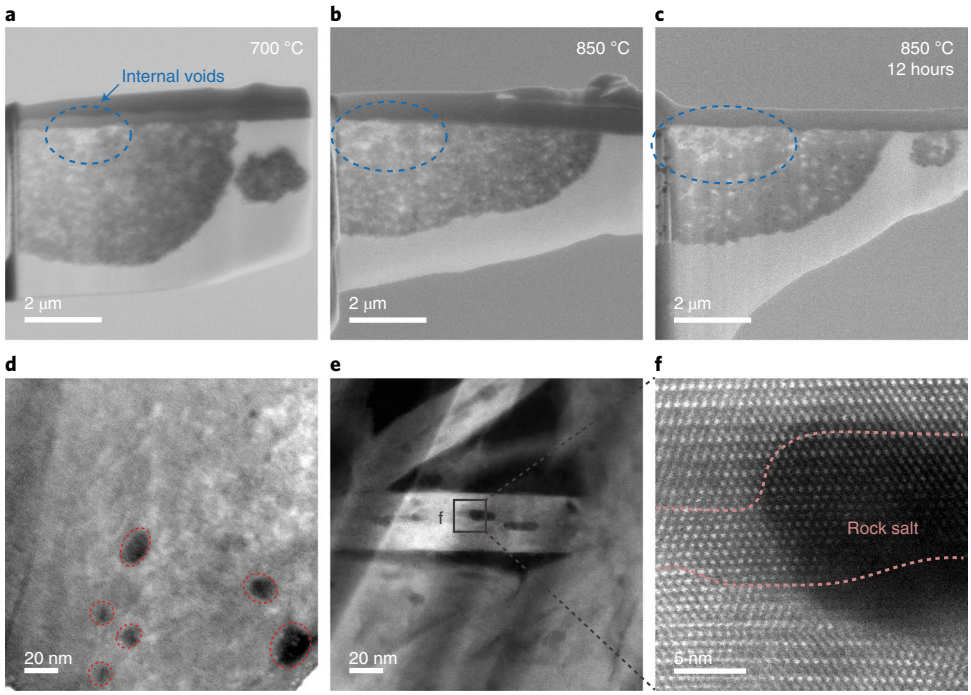

Fig. 3 | Effect of heterogeneity on the final products of layered oxides. a–c, Cross-sectional SEM images of samples annealed to high temperatures of 700 °C (**a**) and 850 °C (**b**), and the final nickel-rich NCM after 12 h sintering at 850 °C (**c**). The blue dotted circle indicates the internal voids that emerge from high temperature. **d**, STEM image of intrinsic nanopores (red dotted circles) on the final product of as-synthesized layered oxide. **e**, TEM image of nanopores in 500 °C heated sample. **f**, Atomic-resolution STEM images of nanopores. The dashed lines indicate the area that we identified as the rock salt phase.

the relative mass starting from 240 °C, whereas the mass reduction is observed in the core region. Although the general mass reduction can be attributed to the dehydration in the whole particle, the relative decrease of the negative intensity observed in the core region presumably originates from the local decrease of particle density. Considering the similar onset temperatures of synthetic lithiation and self-dehydration of the $TM(OH)_2$, it is likely that access by an incoming lithium source to the core of the particle is kinetically restricted. Then, the self-decomposition of the unreacted core accompanies the mass loss, resulting in the sparseness of the core region. These results imply that the core–shell formation is caused by the kinetic competition between two reactions depending on the local accessibility to lithium sources.

We conducted ex situ electron microscopy analysis of the NCM precursor mixtures to further verify the spatial reaction heterogeneity. Figure 2g–i presents the cross-sectional SEM images of mixtures quenched after annealing at 100, 300 and 500 °C. The sample at 100 °C in Fig. 2g retained the particle morphology of the pristine NCM precursor mixtures (Supplementary Fig. 4), indicating the absence of the major reaction. By contrast, after heating at 300 °C, the sample featured a noticeable radial heterogeneity in its compactness, with the core–shell morphology exposed in Fig. 2h and Supplementary Fig. 5, consistent with the in situ TEM observations. Furthermore, the X-ray diffraction refinement result of the 300 °C sample (Fig. 2j) shows the presence of multiple phases including a considerable amount of rock-salt phase, implying the simultaneous thermal decomposition of $TM(OH)_2$ along with the synthetic lithiation.

Further spatially resolved TEM examination of local regions of the 300 °C sample shows that primary particles in the core display seriously damaged textures with rough surfaces and holes (Fig. 2k,l). By contrast, for those in the shell region, the initial precursor morphology was relatively well maintained without the noticeable microscopic defects (Fig. 2n,o). More importantly, the selected area electron diffraction of each region reveals that the core particles mainly consisted of the rock-salt phase (Fig. 2m), whereas the shell particles exhibited a layered structure (Fig. 2p). This observation evidently supports the proposed mechanism that the synthetic lithiation initiating from the interface leads to a layered-to-layered topotactic phase transition at the shell while the intrinsic thermal dehydration of the $TM(OH)_2$ occurs in the core accompanied by the formation of the rock-salt phase. In the morphological point of view, the early synthetic lithiation templates the outer perimeter of the secondary particle, building a rigid and dense shell, and then the subsequent densification of the inner transition-metal compound by self-dehydration with gas evolution results in the sparseness of the core region. The coexistence of lithium-containing and lithium-free phases has been suggested in a recent in situ diffraction study[40]; however, we show that such coexistence originates from the biphasic core–shell structure in single particles. Moreover, electron microscopy analysis on the sample annealed at 500 °C (Fig. 2i and Extended Data Fig. 3) shows that the radial heterogeneity was alleviated to some extent in the aspect of both compactness and phase evolution at this temperature, indicating that the core–shell morphology is an intermediate state temporarily captured during the heat treatment, whose implication will be further discussed later. These results imply that the synthetic reactions are kinetically governed by the lithium diffusion from the outer lithium sources.

Effect of reaction heterogeneity on the final structure. Inspired by the finding on the heterogeneous reaction pathway featuring the core–shell morphology, we further examined the morphological evolution during the final high-temperature sintering process (Fig. 3a–c). The close inspection clarifies that the samples treated at higher temperatures still exhibit a trace of the heterogeneous compactness across the radial direction. More noteworthy is that as the sintering temperature increases, the inhomogeneity in the compactness is translationally displayed with the appearance of the inner void space near the centre of the secondary particle, which becomes

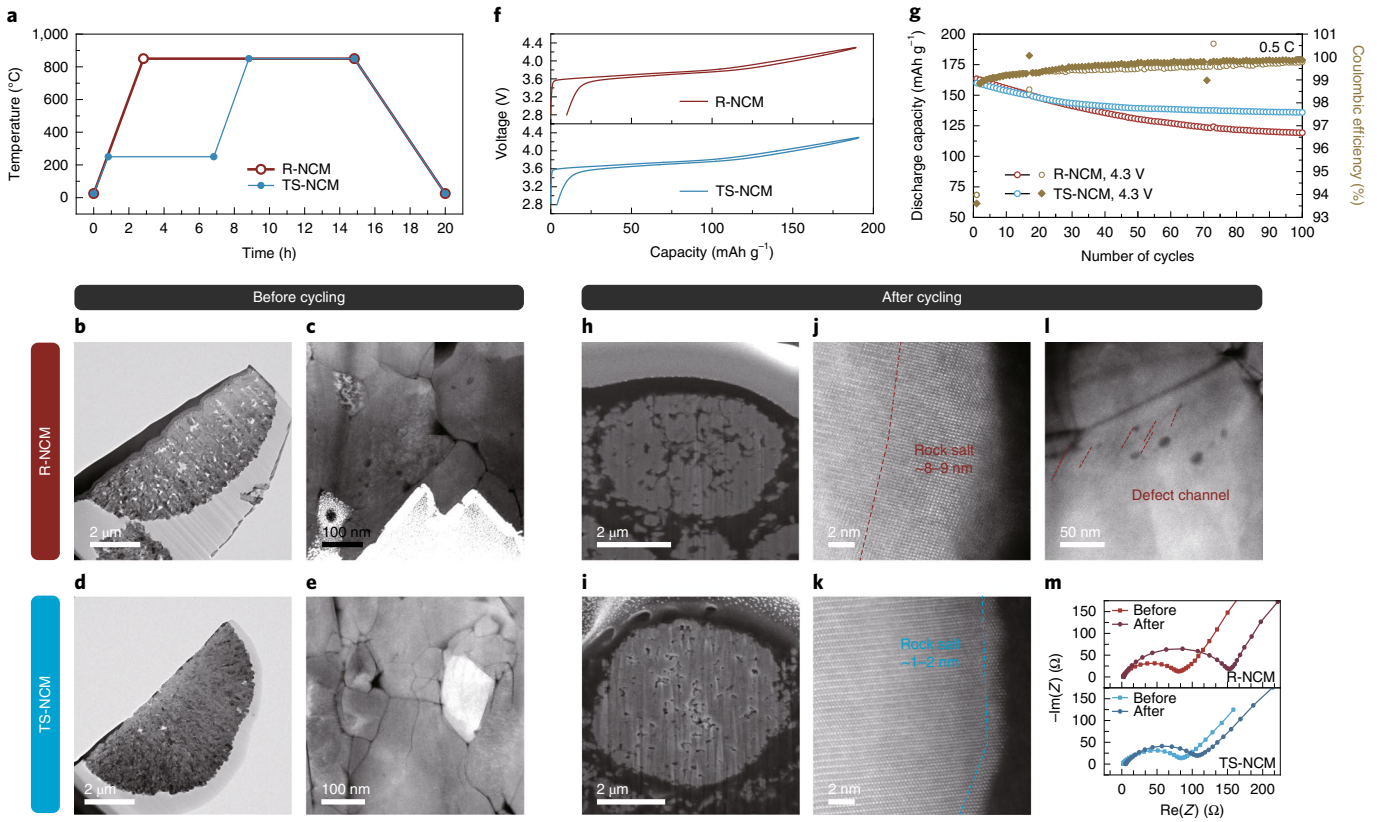

Fig. 4 | Electrochemical properties of NCM layered oxide with two-step calcination. a, Temperature profile for calcination. **b**, Cross-sectional TEM image of R-NCM layered oxide. **c**, STEM image of R-NCM layered oxide. **d**, Cross-sectional TEM image of TS-NCM layered oxide. **e**, STEM image of TS-NCM layered oxide. **f**, Charge/discharge profile of layered oxide at 0.1 C. **g**, Capacity retention and Coulombic efficiency during cycling. **h**,**i**, Cross-sectional SEM image of R-NCM layered oxide (**h**) and TS-NCM layered oxide (**i**). **j**,**k**, Atomic-resolution STEM image of cycled R-NCM layered oxide (**j**) and TS-NCM layered oxide (**k**). **l**, STEM image of channelled nanopore defects. The dashed lines mark the channel between nanopores. **m**, Electrochemical impedance (*Z*) spectroscopy Nyquist plots of cells with NCM layered oxides before and after cycling.

larger with higher temperature. We suppose that the densely packed shell region facilitates earlier particle sintering than does the coarsely packed core region. Therefore, during the sintering of the core particles, they tend to agglomerate towards the outer shell region for continuous growth, leaving intergranular voids in the secondary particles. This finding is consistent with previous observations of internal voids in typical nickel-rich layered oxides[8,18–20].

The nanopore defects in the primary particles were also still observed, particularly in the core region of the secondary particles. The scanning transmission electron microscopy (STEM) images in Fig. 3d,e clearly depict the presence of the nanopore in the primary particles. Interestingly, the crystalline phase near the nanopore (Fig. 3f) was found to be primarily the lithium-deficient rock-salt (NCM-O) structure, in contrast to the rest of the areas, which consisted of the layered structure, which is supported by the slightly more reduced oxidation state of the transition metals at the nanopore (Extended Data Fig. 4). The nanopores are distributed almost exclusively within the inner part of the particle, suggesting that the nanopores originate from the thermal decomposition of the $TM(OH)_2$ precursors in the core. However, it is also possible that nanopores can be generated at the outer region of particle by localized thermal dehydration, if lithium access is heterogeneous or limited[31].

Defect-regulated nickel-rich layered oxide and its properties. We supposed that the formation of intergranular voids and intragranular nanopores could be mitigated by maximally promoting topotactic lithiation throughout the particle before thermal decomposition occurs. Accordingly, we revised the synthesis route by simply applying the additional holding period at the critical temperature of the lithiation (near 200 °C) as shown in Fig. 4a (herein, the NCM622 obtained by the modified two-step synthetic route is referred to as TS-NCM). The validity of this strategy is also discussed in Extended Data Fig. 5 and Supplementary Note 3. By comparison, the reference NCM622 (R-NCM) was synthesized using the conventional heat-treatment route at 850 °C. Supplementary Fig. 6 confirms that both NCM oxides exhibited identical $R\text{-}\bar{3}m$ layered structures with similar structural parameters (Supplementary Tables 1 and 2). First, we attempted to compare the presence of intergranular void and intragranular nanopore formation through extensive TEM examinations. Figure 4b shows that widespread intergranular voids make up a significant portion of the secondary particles in the R-NCM. Moreover, a number of intragranular nanopores can be seen in the core region of the particle (Fig. 4c and Supplementary Fig. 7). By contrast, we found that the TS-NCM resulted in more compact and dense secondary particles with less void space, as shown in Fig. 4d. Importantly, nanopores were also hardly found in the TS-NCM (Fig. 4e and Supplementary Fig. 7), demonstrating the effectiveness of tailored thermal synthesis in avoiding intrinsic structural defects by circumventing the self-decomposing rock-salt formation. The electrochemical properties were subsequently investigated by constructing lithium half-cells. Although they deliver similar discharge capacities of ~180 mAh g^{-1} at 0.1 C (C-rate, where C/*n* stands for charging or discharging a battery for *n* hours), the TS-NCM offered a higher initial Coulombic efficiency, as shown in the voltage

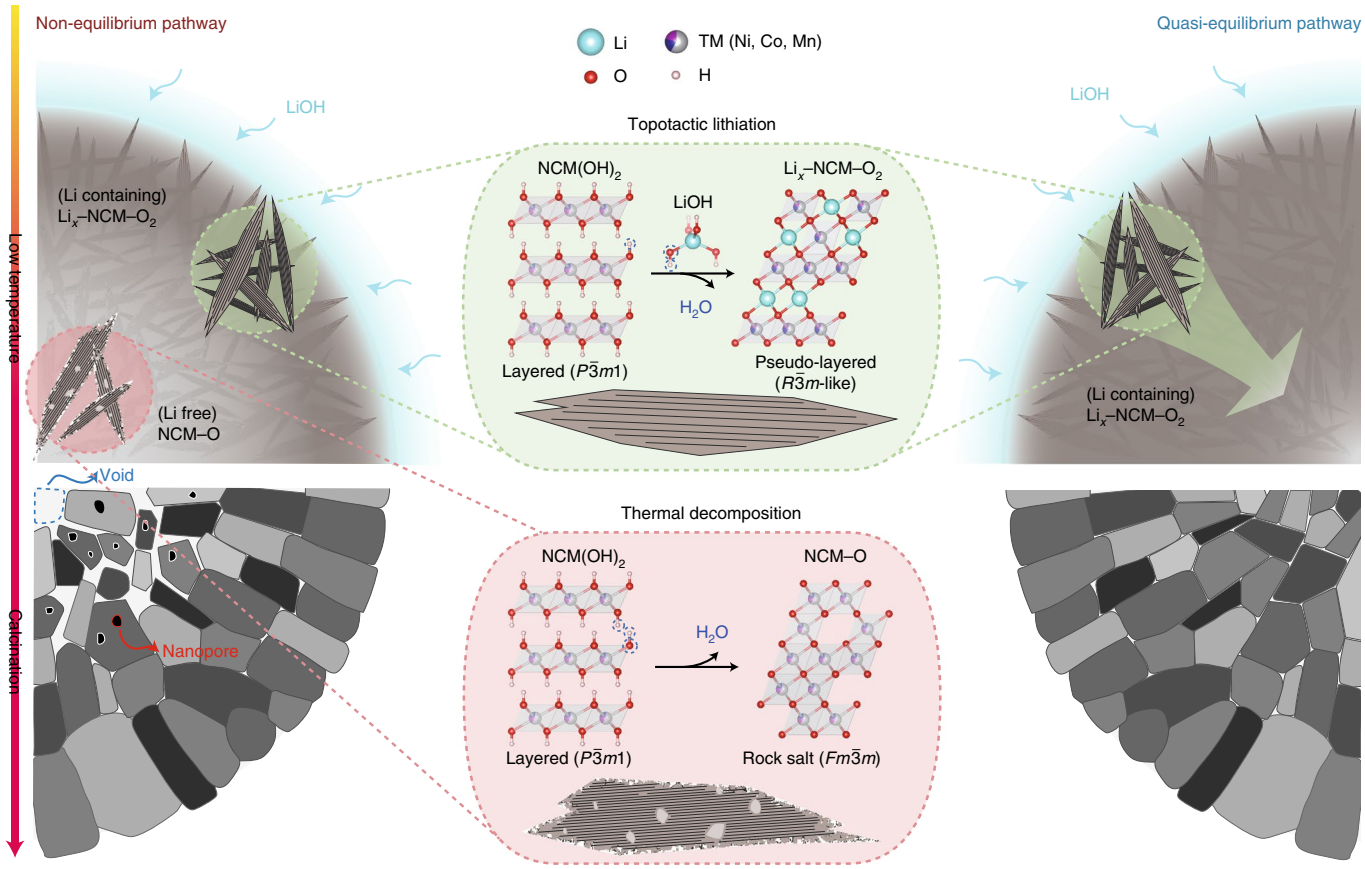

Fig. 5 | Proposed mechanism of reaction heterogeneity during synthesis of nickel-rich layered oxides. Topotactic lithiation at the interface with lithium sources induces early formation of a layered oxide structure, possibly with minor cation disordering or stacking fault formation, leading to morphologically dense and less-changed particles (top centre). The inner-core region with less accessibility for the lithium source drives the thermal decomposition of the $TM(OH)_2$ into the transition-metal oxide with the rock-salt structure, resulting in coarse particle packing with nanopore defects in the primary particles (bottom centre). The generated nanopores remain even after high-temperature sintering. Particle growth and integration proceed in the shell via gradual lithium diffusion and leave void space inside the secondary particles during high-temperature sintering (left). Competitive reactions determine the heterogeneity of the phase evolution within the intermediate state.

profiles for the first cycle (Fig. 4f). As shown in Fig. 4g, the TS-NCM was also capable of delivering a better capacity retention (83% after 100 cycles at 0.5 C) than was the R-NCM (74%). The improved cycle stabilities of the TS-NCM were additionally observed at different cycling rates of 0.1 C and 1 C (Extended Data Fig. 6). It is thus demonstrated that simply adding one low-temperature holding step in the synthesis of the TS-NCM electrode (without doping or coating) results in improved Coulombic efficiencies during the entire cycling duration.

Post-mortem electron microscopy analyses of the cycled electrodes were performed to investigate the degradation behaviour of the electrodes. Figure 4h clearly shows that the R-NCM was mechanically deformed with crack formation involving the inherent void structures; however, the TS-NCM remained relatively intact, preserving the original structural integrity (Fig. 4i). Microcracking generally involves the opening of a new surface of the particles, which is prone to parasitic reactions with the electrolyte and resultant surface reconstructions[13,15,16,50,51]. In particular, when microcracking occurs and connects with intergranular voids, the deterioration of the electrodes is accelerated due to the large open surface along the intergranular void space[20]. Severe side reactions were revealed by high-resolution STEM examinations in the R-NCM, particularly for the core region near voids. A much thicker rock-salt reconstruction layer, ranging from 8 to 10 nm thick, was detected in the cycled R-NCM (Fig. 4j), whereas a relatively intact surface was maintained in the TS-NCM with a thinner rock-salt layer of up to 2 nm (Fig. 4k). As recent works have proposed that the bulk fatigue of nickel-rich cathodes is typically induced by the surface reconstructions, the larger surface reconstruction layers generated along the void spaces in the R-NCM likely induce the faster capacity decay[52].

Interestingly, new defect channels among the nanopores were observed in the core of the cycled R-NCM (red dotted lines in Fig. 4l), confirming the detrimental effect of intrinsic nanopores[26,27,30,31]. The observation on the defect clustering and propagation is complementary to the previous reports that the defect aggregation can also lead to the creation of additional nanopores as a result of electrochemical cycling[30,31]. We suspect that the propagation of defect channels from nanopores also contributed to the deactivation of the electrodes, retarding the transport properties through the defects and nanopores. The electrochemical impedance spectroscopy results in Fig. 4m indicate that these electrode deformations after cycling eventually increase the impedance of the cells. Although both cells exhibited similar charge-transfer impedance (80 Ω) before cycling, the R-NCM showed a notable build-up of impedance, up to 150 Ω, which contrasts with the slight increase to 110 Ω of the TS-NCM after 100 cycles. These results obviously support the idea that strengthening the structural integrity from primary to secondary levels by controlling intrinsic structural defects during the synthesis is of essence to improve the cycle stability of the high-nickel-content

layered electrodes. Our study suggests that further room exists to optimize the synthesis protocol to improve the electrochemical property in combination with previously reported effective remedies including coating[53,54], doping[55,56] and morphology controls[57,58].

Proposed formation mechanism of nickel-rich layered oxides. We propose a mechanism for the interplay between the kinetics and thermodynamics on the morphological evolution of nickel-rich NCM during the solid-state synthesis, as illustrated in Fig. 5. In the synthesis of nickel-rich NCM with LiOH, the synthetic lithiation and the thermal decomposition of the $TM(OH)_2$ could be driven consecutively at the low temperature. When the precursors follow a non-equilibrium pathway, the competitive reactions appear at radially distinct regions of the particle depending on the lithium accessibility, which leads to the core–shell templated intermediate microstructures. Although the reaction heterogeneities do not inhibit the overall layered structure development in the final product, it leaves intergranular voids and intragranular nanopores, resulting in deterioration of the microstructure integrity and consequently of the electrochemical cycle stability. By contrast, the simple modification in the synthetic strategy, especially at low temperature, which allows the quasi-equilibrium pathway to dominate, promotes synthetic lithiation while suppressing the thermal dehydration of TM precursors. The even phase evolution over the secondary particle by the synthetic lithiation leads to uniformly integrated microstructure development with effective suppression of the intergranular voids and intragranular nanopores, aiding in the achievement of enhanced cycle stability of nickel-rich layered oxides.

Conclusion

We explored the real-time solid-state synthetic process of NCM622 using multiscale in situ analysis. We revealed that the kinetic competition between the synthetic lithiation and intrinsic thermal decomposition of the $TM(OH)_2$ governs the solid-state reaction pathway of nickel-rich layered oxides over the secondary particles. Moreover, we found that thermal decomposition in the bulk leads to intrinsic microstructural defects, internal voids and intragranular nanopores, which are detrimental to the electrochemical stability of nickel-rich NCM electrodes. On the basis of the mechanistic understanding of the intertwinement between thermodynamics and kinetics, we proposed a quasi-equilibrium route for the synthesis of nickel-rich NCM to circumvent the self-thermal decomposition. Nickel-rich NCM synthesized using the modified two-step calcination strategy exhibited superior cycle stability, benefiting from the successful suppression of the formation of internal voids and nanopores. This work provides insight into the material synthesis from the perspective of defect engineering based on the simple control of the intermediate phases and is thus expected to expedite the practical development of high-energy nickel-rich layered electrodes for lithium-ion batteries with improved performance and long-term stability.

Online content

Any methods, additional references, Nature Research reporting summaries, source data, extended data, supplementary information, acknowledgements, peer review information; details of author contributions and competing interests; and statements of data and code availability are available at https://doi.org/10.1038/s41557-022-00915-2.

Received: 26 June 2021; Accepted: 23 February 2022;
Published online: 21 April 2022

References

1. Liu, Z., Yu, A. & Lee, J. Y. Synthesis and characterization of $LiNi_{1-x-y}Co_xMn_yO_2$ as the cathode materials of secondary lithium batteries. *J. Power Sources* **81–82**, 416–419 (1999).
2. Noh, H.-J., Youn, S., Yoon, C. S. & Sun, Y.-K. Comparison of the structural and electrochemical properties of layered $Li[Ni_xCo_yMn_z]O_2$ (x = 1/3, 0.5, 0.6, 0.7, 0.8 and 0.85) cathode material for lithium-ion batteries. *J. Power Sources* **233**, 121–130 (2013).
3. Sharma, S. S. & Manthiram, A. Towards more environmentally and socially responsible batteries. *Energy Environ. Sci.* **13**, 4087–4097 (2020).
4. Kim, J. et al. Prospect and reality of Ni-rich cathode for commercialization. *Adv. Energy Mater.* **8**, 1702028 (2018).
5. Li, W., Erickson, E. M. & Manthiram, A. High-nickel layered oxide cathodes for lithium-based automotive batteries. *Nat. Energy* **5**, 26–34 (2020).
6. de Biasi, L. et al. Chemical, structural, and electronic aspects of formation and degradation behavior on different length scales of Ni-rich NCM and Li-rich HE-NCM cathode materials in Li-ion batteries. *Adv. Mater.* **31**, 1900985 (2019).
7. Jung, S.-K. et al. Understanding the degradation mechanisms of $LiNi_{0.5}Co_{0.2}Mn_{0.3}O_2$ cathode material in lithium ion batteries. *Adv. Energy Mater.* **4**, 1300787 (2014).
8. Yan, P., Zheng, J., Zhang, J.-G. & Wang, C. Atomic resolution structural and chemical imaging revealing the sequential migration of Ni, Co, and Mn upon the battery cycling of layered cathode. *Nano Lett.* **17**, 3946–3951 (2017).
9. Zheng, H., Sun, Q., Liu, G., Song, X. & Battaglia, V. S. Correlation between dissolution behavior and electrochemical cycling performance for $LiNi_{1/3}Co_{1/3}Mn_{1/3}O_2$-based cells. *J. Power Sources* **207**, 134–140 (2012).
10. Kim, J. et al. A highly stabilized nickel-rich cathode material by nanoscale epitaxy control for high-energy lithium-ion batteries. *Energy Environ. Sci.* **11**, 1449–1459 (2018).
11. Jung, R., Metzger, M., Maglia, F., Stinner, C. & Gasteiger, H. A. Oxygen release and its effect on the cycling stability of $LiNi_xMn_yCo_zO_2$ (NMC) cathode materials for Li-ion batteries. *J. Electrochem. Soc.* **164**, A1361–A1377 (2017).
12. Mu, L. et al. Oxygen release induced chemomechanical breakdown of layered cathode materials. *Nano Lett.* **18**, 3241–3249 (2018).
13. Li, S. et al. Mutual modulation between surface chemistry and bulk microstructure within secondary particles of nickel-rich layered oxides. *Nat. Commun.* **11**, 4433 (2020).
14. Li, W., Asl, H. Y., Xie, Q. & Manthiram, A. Collapse of $LiNi_{1-x-y}Co_xMn_yO_2$ lattice at deep charge irrespective of nickel content in lithium-ion batteries. *J. Am. Chem. Soc.* **141**, 5097–5101 (2019).
15. Romano Brandt, L. et al. Synchrotron X-ray quantitative evaluation of transient deformation and damage phenomena in a single nickel-rich cathode particle. *Energy Environ. Sci.* **13**, 3556–3566 (2020).
16. Xu, Z. et al. Charge distribution guided by grain crystallographic orientations in polycrystalline battery materials. *Nat. Commun.* **11**, 83 (2020).
17. Tian, C. et al. Charge heterogeneity and surface chemistry in polycrystalline cathode materials. *Joule* **2**, 464–477 (2018).
18. Xiao, B. et al. Revealing the atomic origin of heterogeneous Li-ion diffusion by probing Na. *Adv. Mater.* **31**, 1805889 (2019).
19. Heenan, T. M. M. et al. Resolving Li-ion battery electrode particles using rapid lab-based X-ray nano-computed tomography for high-throughput quantification. *Adv. Sci.* **7**, 2000362 (2020).
20. Mao, Y. et al. High-voltage charging-induced strain, heterogeneity, and micro-cracks in secondary particles of a nickel-rich layered cathode material. *Adv. Funct. Mater.* **29**, 1900247 (2019).
21. Lin, F. et al. Surface reconstruction and chemical evolution of stoichiometric layered cathode materials for lithium-ion batteries. *Nat. Commun.* **5**, 3529 (2014).
22. Zhu, J. et al. Atomic-level understanding of surface reconstruction based on $Li[Ni_xMn_yCo_{1-x-y}]O_2$ single-crystal studies. *ACS Appl. Energy Mater.* **3**, 4799–4811 (2020).
23. Duan, Y. et al. Insights into Li/Ni ordering and surface reconstruction during synthesis of Ni-rich layered oxides. *J. Mater. Chem. A* **7**, 513–519 (2019).
24. Zhang, H. et al. Facet-dependent rock-salt reconstruction on the surface of layered oxide cathodes. *Chem. Mater.* **30**, 692–699 (2018).
25. Zhang, M.-J. et al. Cooling induced surface reconstruction during synthesis of high-Ni layered oxides. *Adv. Energy Mater.* **9**, 1901915 (2019).
26. Ahmed, S. et al. The role of intragranular nanopores in capacity fade of nickel-rich layered $Li(Ni_{1-x-y}Co_xMn_y)O_2$ cathode materials. *ACS Nano* **13**, 10694–10704 (2019).
27. Pokle, A. et al. In situ monitoring of thermally induced effects in nickel-rich layered oxide cathode materials at the atomic level. *ACS Appl. Mater. Interfaces* **12**, 57047–57054 (2020).
28. Shukla, A. K. et al. Unravelling structural ambiguities in lithium- and manganese-rich transition metal oxides. *Nat. Commun.* **6**, 8711 (2015).
29. Yan, P. et al. Ni and Co segregations on selective surface facets and rational design of layered lithium transition-metal oxide cathodes. *Adv. Energy Mater.* **6**, 1502455 (2016).
30. Li, L., Hu, J., Xiao, J. & Wang, C. Origin, nature, and the dynamic behavior of nanoscale vacancy clusters in Ni-rich layered oxide cathodes. *ACS Appl. Mater. Interfaces* **13**, 18849–18855 (2021).

31. Lin, R. et al. Hierarchical nickel valence gradient stabilizes high-nickel content layered cathode materials. *Nat. Commun.* **12**, 2350 (2021).
32. Qian, G. et al. Single-crystal nickel-rich layered-oxide battery cathode materials: synthesis, electrochemistry, and intra-granular fracture. *Energy Storage Mater.* **27**, 140–149 (2020).
33. Zhang, F. et al. Surface regulation enables high stability of single-crystal lithium-ion cathodes at high voltage. *Nat. Commun.* **11**, 3050 (2020).
34. Shim, J.-H. et al. Effects of heat-treatment atmosphere on electrochemical performances of Ni-rich mixed-metal oxide ($LiNi_{0.80}Co_{0.15}Mn_{0.05}O_2$) as a cathode material for lithium ion battery. *Electrochim. Acta* **138**, 15–21 (2014).
35. Wang, D. et al. Synthetic control of kinetic reaction pathway and cationic ordering in high-Ni layered oxide cathodes. *Adv. Mater.* **29**, 1606715 (2017).
36. Zhao, J. et al. In situ probing and synthetic control of cationic ordering in Ni-rich layered oxide cathodes. *Adv. Energy Mater.* **7**, 1601266 (2017).
37. Zhang, M.-J. et al. Cationic ordering coupled to reconstruction of basic building units during synthesis of high-Ni layered oxides. *J. Am. Chem. Soc.* **140**, 12484–12492 (2018).
38. Bai, J. et al. Kinetic pathways templated by low-temperature intermediates during solid-state synthesis of layered oxides. *Chem. Mater.* **32**, 9906–9913 (2020).
39. Bianchini, M. et al. The interplay between thermodynamics and kinetics in the solid-state synthesis of layered oxides. *Nat. Mater.* **19**, 1088–1095 (2020).
40. Hua, W. et al. Chemical and structural evolution during the synthesis of layered $Li(Ni,Co,Mn)O_2$ oxides. *Chem. Mater.* **32**, 4984–4997 (2020).
41. Wang, S. et al. Kinetic control of long-range cationic ordering in the synthesis of layered Ni-rich oxides. *Adv. Funct. Mater.* **31**, 2009949 (2021).
42. Maier, J. Thermodynamics of electrochemical lithium storage. *Angew. Chem. Int. Ed.* **52**, 4998–5026 (2013).
43. Li, Y. et al. Synthesis of full concentration gradient cathode studied by high energy X-ray diffraction. *Nano Energy* **19**, 522–531 (2016).
44. Dong, B. et al. One-step synthesis of free-standing α-$Ni(OH)_2$ nanosheets on reduced graphene oxide for high-performance supercapacitors. *Nanotechnology* **25**, 435403 (2014).
45. Wang, D., Xu, R., Wang, X. & Li, Y. NiO nanorings and their unexpected catalytic property for CO oxidation. *Nanotechnology* **17**, 979–983 (2006).
46. Abbas, S. A., Iqbal, M. I., Kim, S.-H., Abbas Khan, H. & Jung, K.-D. Facile synthesis of alfa-nickel hydroxide by an ultrasound-assisted method and its application in energy storage devices. *Appl. Surf. Sci.* **474**, 218–226 (2019).
47. Liu, Q. et al. Approaching the capacity limit of lithium cobalt oxide in lithium ion batteries via lanthanum and aluminium doping. *Nat. Energy* **3**, 936–943 (2018).
48. Seong, W. M. et al. Abnormal self-discharge in lithium-ion batteries. *Energy Environ. Sci.* **11**, 970–978 (2018).
49. Zhang, J.-N. et al. Trace doping of multiple elements enables stable battery cycling of $LiCoO_2$ at 4.6 V. *Nat. Energy* **4**, 594–603 (2019).
50. Nam, G. W. et al. Capacity fading of Ni-rich NCA cathodes: effect of microcracking extent. *ACS Energy Lett.* **4**, 2995–3001 (2019).
51. Liu, X. et al. Essential effect of the electrolyte on the mechanical and chemical degradation of $LiNi_{0.8}Co_{0.15}Al_{0.05}O_2$ cathodes upon long-term cycling. *J. Mater. Chem. A* **9**, 2111–2119 (2021).
52. Xu, C. et al. Bulk fatigue induced by surface reconstruction in layered Ni-rich cathodes for Li-ion batteries. *Nat. Mater.* **20**, 84–92 (2021).
53. Yan, P. et al. Tailoring grain boundary structures and chemistry of Ni-rich layered cathodes for enhanced cycle stability of lithium-ion batteries. *Nat. Energy* **3**, 600–605 (2018).
54. Yoon, M. et al. Reactive boride infusion stabilizes Ni-rich cathodes for lithium-ion batteries. *Nat. Energy* **6**, 362–371 (2021).
55. Zou, L. et al. Lattice doping regulated interfacial reactions in cathode for enhanced cycling stability. *Nat. Commun.* **10**, 3447 (2019).
56. Jung, C.-H. et al. Revisiting the role of Zr doping in Ni-rich layered cathodes for lithium-ion batteries. *J. Mater. Chem. A* **9**, 17415–17424 (2021).
57. Kim, U.-H. et al. Heuristic solution for achieving long-term cycle stability for Ni-rich layered cathodes at full depth of discharge. *Nat. Energy* **5**, 860–869 (2020).
58. Jung, C.-H. et al. New insight into microstructure engineering of Ni-rich layered oxide cathode for high performance lithium ion batteries. *Adv. Funct. Mater.* **31**, 2010095 (2021).

Methods

Materials. Powdery mixtures of the transition-metal hydroxide and lithium compounds were supplied by Samsung SDI. The mixture powders were heated following a given temperature profile with a ramping rate of 5 °C min^{-1} and then naturally cooled to room temperature with the oxygen gas flowing at 2 ml min^{-1}. The final R-NCM materials were prepared by annealing at 850 °C for 12 h at a ramping rate of 5 °C min^{-1}. We prepared TS-NCM materials by consecutive calcination at 250 °C for 6 h and 850 °C for 6 h.

Characterization. In situ heating X-ray diffraction measurements were conducted in the 2θ range of 10–70° with a step size of 0.013° and step time of 0.25 s using an X-ray diffractometer (Empyrean, Malvern Panalytical) equipped with Cu Kα radiation (wavelength $\lambda = 1.540598$ Å) at the Korea Atomic Energy Research Institute. In situ heating X-ray diffraction data were collected with oxygen flowing at 2 ml min^{-1} while heating the samples at a ramping rate of 5 °C min^{-1} and relaxing for 5 min before the measurements at each given temperature. Ex situ powder X-ray diffraction patterns were obtained in the 2θ range of 10–70° with a step size of 0.005° and step time of 3 s using an X-ray diffractometer (New D8 Advance, Bruker). High-resolution powder diffraction analysis was also performed for the prepared NCM powders at beamline 9B at the Pohang Light Source at the Pohang Accelerator Laboratory, Republic of Korea. The high-resolution powder diffraction pattern was recorded over the 2θ range of 10–130° with a step size of 0.01°, step time of 3 s and wavelength of $\lambda = 1.5226$ Å. Rietveld refinements were performed using the FullProf program based on the diffraction patterns. We adopted a conventional structural model of $(Li_{1-x}Ni_x)(Li_xNi_{0.6-x}Co_{0.2}Mn_{0.2})O_2$ ($R\text{-}\bar{3}m$ space group with Li–Ni intermixing) for Rietveld refinement of diffraction data of layered oxide materials[31,52,59]. Discussions on the validity of the refinement results and phase analysis model are provided in Supplementary Fig. 8. Thermal analyses were performed using a simultaneous DTA–TGA analyser (SDT, TA instruments).

Electron microscopy. In situ TEM experiments with gas-cell heating were performed using a commercially available holder and chips (DENSsolutions, Climate, Gas flow and heating system). The gas cell consisted of a bottom chip (30 nm Si_3N_4 membrane) and a top chip (50 nm Si_3N_4 membrane). The electrodes are patterned on the bottom chip near the window to generate a uniform heating environment inside the gas cell. For the clear visualization of the interfacial reaction, a two-dimensional lamella type of precursor sample was manufactured using a focused ion beam system, where the $TM(OH)_2$ particle was surrounded by LiOH, as illustrated in Fig. 2a. The focused ion beam lamella was prepared from a pelletized mixture of $NCM(OH)_2$ and LiOH with a molar ratio of 1:10 and was carefully loaded on the bottom chip without breaking the membrane (Supplementary Fig. 9 and Supplementary Note 4). The oxygen atmosphere was creating by oxygen flow generating 1 bar pressure inside the cell. The synthesis was conducted at a ramping rate of 6 °C min^{-1} up to 850 °C. The in situ TEM experiment was performed on a JEOL JEM 2100F equipped with 2k (2,048) × 2k (2,048) Gatan UltraScan 1000 operated at 200 kV, installed at the Korea Institute of Materials Science. TEM images were acquired every 10 °C up to 500 °C using an ~4.8 e^- $Å^{-2}$ s^{-1} dose rate (e^-, electron) with 0.2 s exposure time to avoid beam damage of LiOH, and a video was acquired after LiOH was decomposed at a dose rate of 7.344 e^- $Å^{-2}$ s^{-1}. The defocus value was fixed during all the imaging. The TEM images provided in Fig. 2c are colour-coded using the colour table in ImageJ, each value from 0 to 255. All the focused ion beam samples were prepared using the Thermo Fischer Helios G4 installed at the Korea Basic Science Institute and the NOVA 200 installed at the National NanoFab Center. Cross-sectional SEM images were obtained using a FEI NOVA 200 after focused ion beam preparation. TEM images, selected area electron diffraction patterns, NBD patterns and high-angle annular dark-field STEM images were obtained on a JEOL JEM 2100F equipped with 1k (1,024) × 1k (1,024) Gatan UltraScan 1000 operated at 200 kV, installed at the Institute for Basic Science (Seoul National University). The high-resolution STEM images were obtained using a Cs-corrected JEOL ARM200F at 200 kV, installed at the National Center for Inter-university Research Facilities (Seoul National University), and a Cs-corrected Thermo Fischer Themis Z at 300 kV, installed at the Research Institute of Advanced Materials (Seoul National University). STEM electron energy-loss spectroscopy data were collected with a dispersion of 0.25 eV per channel and a collection angle of 39.6 mrad using the Cs-corrected JEOL ARM200F operated at 200 kV.

Electrochemical measurements. The electrodes were fabricated by casting a slurry of active materials, carbon black (Super P) and polyvinylidene fluoride binder with a mass ratio of 8:1:1 dissolved in *N*-methyl-2-pyrrolidone (99.5%, Sigma-Aldrich) on aluminium foil. The cast electrode was dried in a 70 °C vacuum oven overnight to dry out the *N*-methyl-2-pyrrolidone solvent. The average loading mass of the electrode was ~2 mg cm^{-2}. Coin-type cells (CR2032, Hohsen) were assembled by stacking a half-inch-diameter electrode, a slice of glass-fibre filter separator (grade GF/F filter, Whatman) and a lithium metal foil in an Ar-filled glove box. The separator was soaked with electrolyte consisting of a 1.0 M solution of $LiPF_6$ in a mixture of ethyl carbonate and dimethyl carbonate (1:1 v/v). Galvanostatic charge/discharge testing was performed in the voltage range of 2.7–4.3 V at room temperature using a potentio-galvanostat (WBCS 3000, WonA Tech). Electrochemical impedance measurements were performed using a potentio-galvanostat (VSP-300, Bio-Logic Science Instruments) at room temperature in the frequency range of 200 kHz to 50 mHz.

Data availability

All the data supporting the findings of this study are available within the article and its Supplementary Information and also from the corresponding authors upon reasonable request. Source data are provided with this paper.

Code availability

The code for calculation of particle average TEM intensity is available at https://github.com/parkhayoungg/Parklab_nchem_NCM_code.

References

59. Song, S. H. et al. High-voltage-driven surface structuring and electrochemical stabilization of Ni-rich layered cathode materials for Li rechargeable batteries. *Adv. Energy Mater.* **10**, 2000521 (2020).

Acknowledgements

This work was supported by the Institute of Basic Science (IBS-R006-A2 and IBS-R006-D1) and by the Defense Challengeable Future Technology Program of the Agency for Defense Development, Republic of Korea (contract no. UC190025RD); financially supported by SK Innovation; and supported by a National Research Foundation of Korea grant funded by the Korean government's Ministry of Science and ICT (no. 2021R1C1C2012688). K.K. acknowledges support from Samsung SDI. Hayoung Park, S.K., J.K. and J.P. acknowledge National Research Foundation of Korea grants, funded by the Korean government's Ministry of Science and ICT (no. NRF-2017R1A5A1015365, no. NRF-2021M3H4A1A02045962 and no. NRF-2020R1A2C2101871). Hayoung Park, Y.J. and J.P. acknowledge support by the Samsung Research Funding & Incubation Center of Samsung Electronics under project no. SRFC-MA2002-03 for the development of the in situ TEM method. K.S. acknowledges the work at the Korea Institute of Materials Science by the Fundamental Research Program of the Korea Institute of Materials Science (grant no. PNK8450).

Author contributions

Hyeokjun Park, Hayoung Park, J.P. and K.K. conceived the original idea and designed the research project. Hyeokjun Park and Hayoung Park carried out the synthesis and the structural and electrochemical characterizations of the materials; participated in all experiments and relevant analyses; and led the project direction. K.S. conducted the in situ heating environment TEM imaging experiments. S.H.S. and H.K. performed the in situ heating X-ray diffraction measurements and provided constructive advice on the analysis of the diffraction results. S.K. conducted the focused ion beam preparation and the high-resolution TEM and high-resolution STEM imaging experiments. K.-H.K., D.E., Y.J., J.K. and W.M.S. offered valuable comments and discussion on the experimental design and analyses. Hyeokjun Park, Hayoung Park, J.P. and K.K. wrote the manuscript with the help of the other authors. The manuscript reflects the contributions of all authors. J.P. and K.K. supervised all aspects of the research.

Competing interests

The authors declare no competing interests.

Additional information

Extended data is available for this paper at https://doi.org/10.1038/s41557-022-00915-2.

Supplementary information The online version contains supplementary material available at https://doi.org/10.1038/s41557-022-00915-2.

Correspondence and requests for materials should be addressed to Jungwon Park or Kisuk Kang.

Peer review information *Nature Chemistry* thanks Jianming Bai, Helmut Ehrenberg, Kerstin Volz and the other, anonymous, reviewer(s) for their contribution to the peer review of this work.

Reprints and permissions information is available at www.nature.com/reprints.

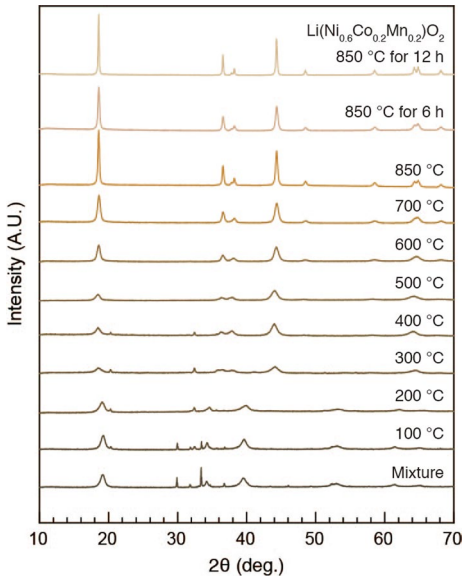

Extended Data Fig. 1 | *Ex situ* XRD pattern of the mixture of transition-metal hydroxide and lithium hydroxide with heating. The *ex situ* samples were collected at different temperatures following the heating profiles of the conventional synthesis of NCM622. Note that the $TM(OH)_2$ is a CdI_2-type layered structure in the $P\bar{3}m1$ space group whose main Bragg reflection appears near 19.5°.

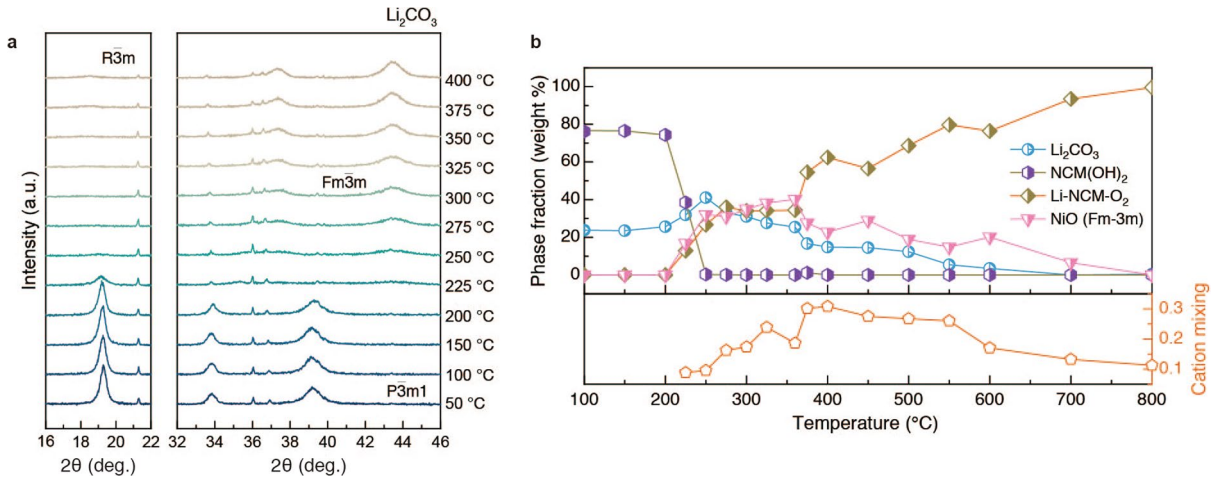

Extended Data Fig. 2 | *In situ* XRD pattern of the mixture of transition-metal hydroxide and lithium carbonate. (**a**) In situ XRD pattern at given equilibrated temperature for calcinations of precursor for layered oxide. (**b**) Phase and structural evolution during the synthesis. The phase fraction of Li_2CO_3 might be overestimated at the certain temperature region near 250 °C because of the decrease in the overall crystallinity of mixed transition metal compounds that undergo the decomposition. Nevertheless, the phase analysis result clearly verifies the distinct synthetic mechanism with the usage of Li_2CO_3 by which thermal dehydration of NCM hydroxide precursor is preceded into the oxide phase, followed by synthetic reaction with Li_2CO_3 at a much higher temperature, resulting in slow formation of layered oxide structures.

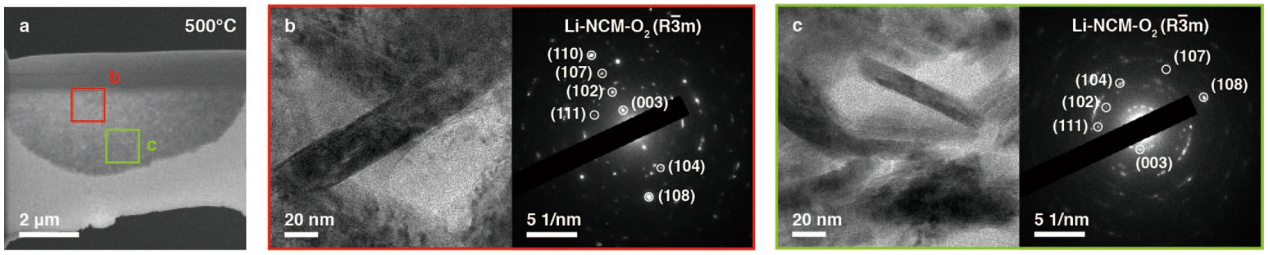

Extended Data Fig. 3 | Cross-sectional SEM and TEM images of transition-metal hydroxide mixture with lithium hydroxide heated *ex situ* at 500 °C. (**a**) Cross-sectional SEM image. TEM images and SAED pattern of primary particles at the (**b**) core and (**c**) shell region, as marked in (a). The radial heterogeneity was alleviated to some extent, which agrees with the results of the negative intensity difference at higher temperature (> 340 °C) in Fig. 2f. The SAED patterns on the sample also indicate that both the core and surface regions of the particle evolved to the lithium-containing layered oxide. This result suggests that the continuous inward supply of lithium through the interface could induce the full lithiation within the secondary particle at this temperature, although the path toward the layered structure formation differs for the shell and core regions.

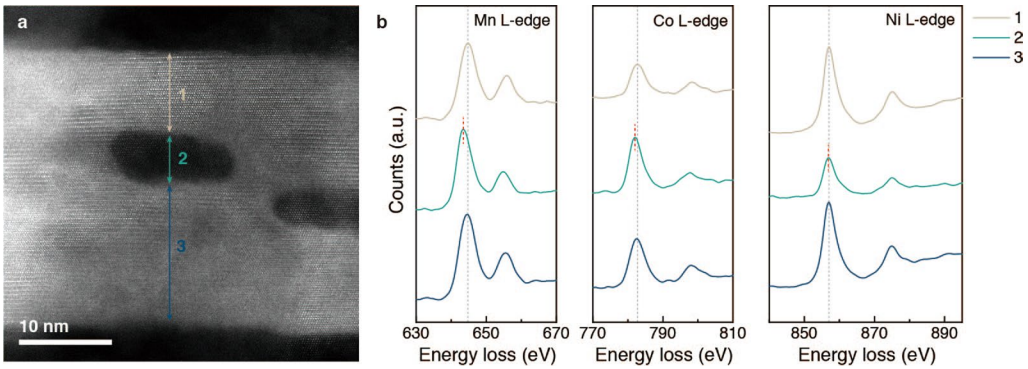

Extended Data Fig. 4 | EELS line scan results of nanopore in transition-metal hydroxide heated at 500 °C. (**a**) STEM image of nanopore within primary particle, (**b**) EELS Mn L-edge, Co L-edge, and Ni L-edge in corresponding area. The oxidation state of the transition metal in the nanopore was slightly more reduced, corresponding to the typical transition-metal states in the rock-salt phase.

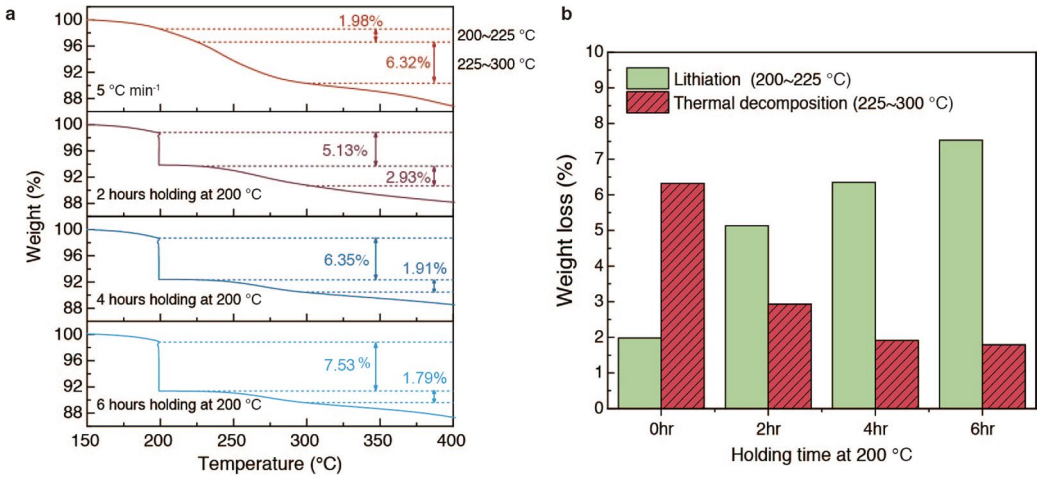

Extended Data Fig. 5 | TG analysis results for mixture of transition-metal hydroxide and lithium hydroxide. (**a**) TG curve with different holding times at 200 °C to 6 h with a heating rate of 5 °C min−1. (**b**) Column graph showing the percentage of weight loss from lithiation and dehydration of transition-metal hydroxide as a function of holding time. Each weight loss is derived from the value measured at 200–225 °C (before 225 °C) and 225–300 °C (after 225 °C) for lithiation and dehydration, respectively. The temperature of 225 °C corresponds to the local minimum point between the two peaks in the TG curve. We set the maximum of the temperature range for thermal dehydration to 300 °C, beyond which negligible thermal activity is observed in the TG curve for the mixture of transition-metal hydroxide and lithium hydroxide. The inversely proportional relationship of the weight loss for the two events indicates that it is reasonable that as much synthetic lithiation as possible occurs. The amount of remaining transition-metal hydroxide precursor that can be thermally decomposed is reduced.

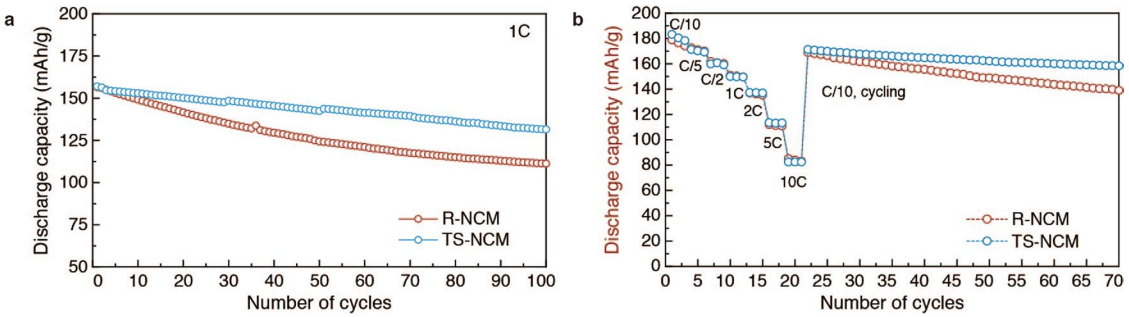

Extended Data Fig. 6 | Electrochemical properties of NCM electrodes at different rates. (**a**) Capacity retention at 1C. (**b**) Rate capability and capacity retention at 0.1C.